Real-Time X-Ray Transmission Microscopy of Solidifying Al-In Alloys

PETER A. CURRERI and WILLIAM F. KAUKLER

Real-time observations of transparent analog materials have provided insight, yet the results of these observations are not necessarily representative of opaque metallic systems. In order to study the detailed dynamics of the solidification process, we develop the technologies needed for real-time X-ray microscopy of solidifying metallic systems, which has not previously been feasible with the necessary resolution, speed, and contrast. In initial studies of Al-In monotectic alloys unidirectionally solidified in an X-ray transparent furnace, *in situ* records of the evolution of interface morphologies, interfacial solute accumulation, and formation of the monotectic droplets were obtained for the first time: A radiomicrograph of Al-30In grown during aircraft parabolic maneuvers is presented, showing the volumetric phase distribution in this specimen. The benefits of using X-ray microscopy for postsolidification metallography include ease of specimen preparation, increased sensitivity, and three-dimensional analysis of phase distribution. Imaging of the solute boundary layer revealed that the isoconcentration lines are not parallel (as is often assumed) to the growth interface. Striations in the solidified crystal did not accurately decorate the interface position and shape. The monotectic composition alloy under some conditions grew in an uncoupled manner.

I. INTRODUCTION

UNAMBIGUOUS testing of current alloy solidification models[1] requires precise knowledge of the shape and extent of the solute boundary layer, real growth rate, solid/liquid interfacial morphology, as well as the nucleation, coalescence, and incorporation into the solid of the phases. Experiments that rely on postsolidification microstructural and compositional analysis provide only an indirect assessment of these critical variables. Interfacial marking techniques such as Peltier pulsing[2] can disturb the solidification processes. Interface quenching[3] gives data only at the time of interruption of the solidification process.

Due to sedimentation processes of one liquid phase within another, the microstructure of monotectic alloys or immiscibles can be strongly influenced by gravity. As a result, there has been much interest in microgravity solidification[4–14] with immiscibles. Curreri and Kaukler[8,13] studied Al-In-Sn monotectic alloys solidified on aircraft (KC-135) during parabolic flight trajectories. Most strikingly, periodic clusters of second-phase particles, as well as compositional and alignment variances in the microstructure, were related to the acceleration modulation. These observations were all from conventional metallographic analysis.

Wu *et al.*[9,13] sectioned an Al-In-Sn specimen into small segments representing high- *vs* low-gravity levels and measured the superconducting transition temperature (about 7.5 K) for each sample. A constant 1 deg variation in the transition temperature was found to consistently correlate with the imposed gravity level. Optical microscopy could not reveal microstructural differences between these segments. However, wavelength dispersive X-ray analysis showed a variation in Sn distribution within the precipitate particles among the sections that correlated to the gravity level during solidification.

Qualitative progress in understanding critical solidification phenomena involved in microstructural evolution has been achieved by the use of transparent organic or salt models.[14,15,16] But the phase structures of the optically transparent systems are often simplified, and their thermophysical and transport properties differ significantly from metallic systems. Thus, there is a fundamental need for experimental techniques that can monitor these phenomena precisely, in real time during the solidification of opaque metal systems.

Electron microscopy of the solidifying surface of thin metal films[17] offers good resolution but is limited to the study of the surface, ignoring important bulk fluid and interfacial phenomena. X-ray transmission microscopy has been employed to study thick specimens (of the order of millimeters) in selected-environments[18] but has until recently lacked the resolution and contrast necessary for it to be an important tool for the study of microscopic solidification fundamentals. Only recently have high resolution X-ray sources and high contrast X-ray detectors advanced enough to allow the systematic study of the relationship between melt dynamics and the resulting microstructure. Synchrotron white beam X-ray sources are being used for X-ray diffraction topography studies of melt/solid interfacial morphology,[19] defect growth,[20] and faceting.[21] Although this technique provides good resolution, it relies on lattice diffraction which cannot be used to image the solute profile or concentration.

X-ray transmission (or shadow) microscopy (XTM) relies on the differential adsorption of the X-ray beam to provide contrast and thus has potential to image concentration gradients in the solid and liquid. Sources allowing resolution of 300 to 500 μm have been used effectively to image

PETER A. CURRERI, Metals and Alloys Group Lead and USMP Mission Scientist, is with the Space Science Laboratory, NASA, Marshall Space Flight Center, AL 35812. WILLIAM F. KAUKLER, Assistant Research Professor, is with the Center for Microgravity and Materials Research, The University of Alabama in Huntsville, Huntsville, AL 35899.

Manuscript submitted March 31, 1995.

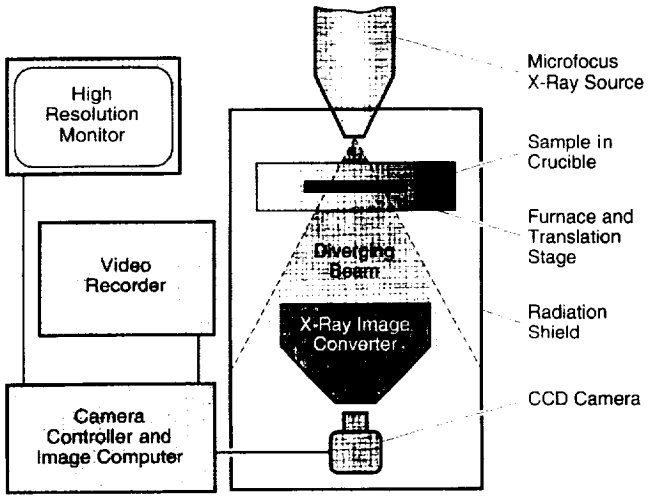

Fig. 1—Schematic diagram of the components for the X-ray transmission microscope.

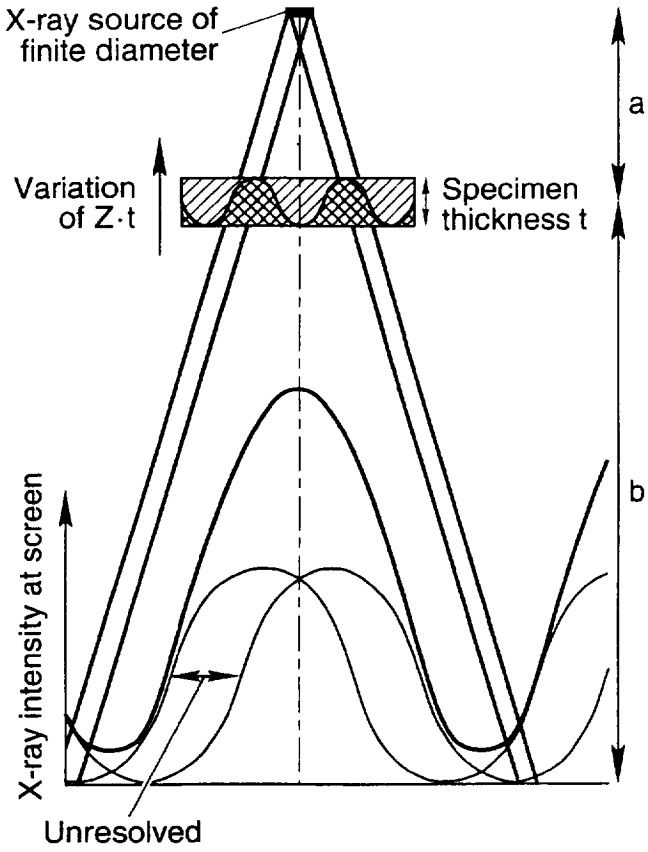

Fig. 2—Projection microscopy concept. The spot size of the source limits the resolution of the image, as shown by the overlapping projections from the extremes of the spot diameter.

shrinkage porosity during aluminum solidification,[22] melt solid interface shape during Bridgman growth of germanium,[23] and the convection caused by dissolving gold and silver wires in liquid sodium.[24] However, the imaging of the most critical microstructural features requires resolution of 1 to 100 μm. An X-ray source capable of this resolution, but with less flux than optimal for metals, has been used[25] to determine the concentration gradients of zinc ions in aqueous solutions during electroplating.

X-ray transmission microscopy is also a valuable tool for postsolidification metallography. Without the furnace housing to limit magnification, specimen examination is possible with higher magnification (over 800 times), high resolution and contrast since the specimen can be placed close to the source, and longer exposures used to achieve higher signal-to-noise ratios. Distribution of solute and solidification features within the specimen volume can be viewed without sectioning or other treatment when the solute has sufficiently higher atomic mass than the solvent. We have applied a state-of-the-art submicron source, capable of 10 to 100 keV acceleration energies, to image *via* XTM the solidification of alloys in real time with resolutions of up to 70 μm[26] and recently to 30 μm. We have successfully imaged solidifying aluminum alloys in real time: interfacial morphologies, coalescence, incorporation of phases into the growing interface, and the solute boundary layer in the liquid at the solid-liquid interface. We have also measured true local growth rates and can evaluate segregation structures in the solid.

II. EXPERIMENTAL APPARATUS AND METHODS

The apparatus employed for this study of the solidification of monotectic Al-In has been described in detail elsewhere.[26] A brief description of the apparatus and method follows.

The use of X-rays for studies of solidification has previously resulted in worthwhile but limited results due to low resolution and image contrast.[19-25] Contact radiography offers both high resolution and contrast, but the method cannot be applied to viewing a dynamic solid-liquid metal interface.

Projection radiography (Figure 1) using a microfocus X-ray source offers magnification, adequate resolution, and (with suitable detector technology) adequate contrast. Superior results can be obtained by using a transmission style target (where accelerated electrons are focused on a thin tungsten film to emit a forward scattered X-ray beam).

Resolution, which is limited by the X-ray spot size (Figure 2), can approach micrometer values. The magnification, M, at the image converter is given by

$$M = (a + b)/a \qquad [1]$$

where a is the distance from the source to the sample and b is the distance from the sample to the detector. For specimens very close to the source, we can obtain magnifications of over 800 times. However, the slope of the instrument magnification curve with distance close to the source is steep and can result in a significant difference in feature magnification through a sample. For our solidification experiments, we selected magnifications in the low range of 5 to 20 times. This resulted in an 8 pct maximum difference in magnification in our 1-mm-thick specimens. Depth information for isolating features in the specimen was obtained by making small lateral adjustments in the relative source/sample position. The nearby features shifted in greater proportion to those farther away from the source. Real-time observations while translating revealed depth structure without resorting to stereoimaging methods. Ster-

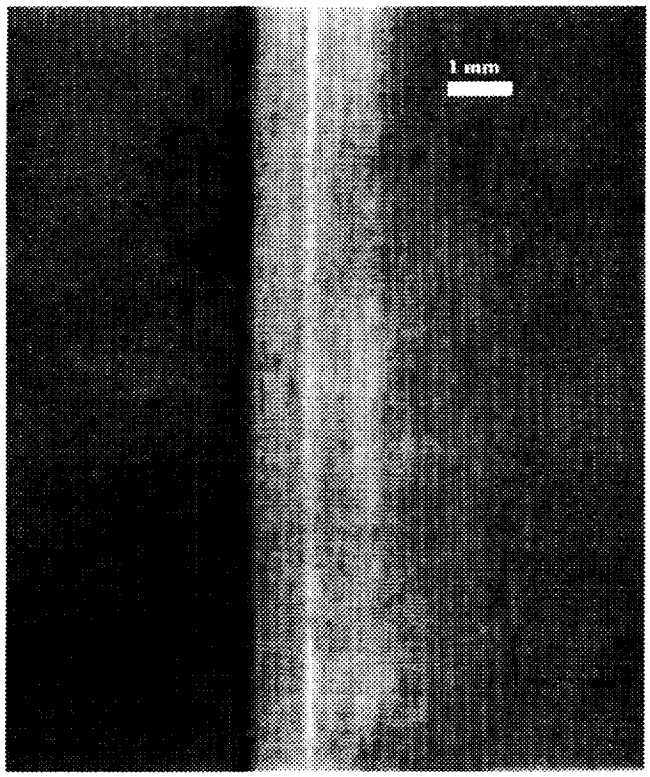

Fig. 3—Al-18In specimen radiomicrograph showing the solid/liquid interface and the light band of Al formed when the interface stagnated at that point after melt-back. The material on the rightmost side is the unmelted parent metal. L_2 droplets (indium-rich liquid) are seen forming in the melt near the solid/liquid interface. The thermal gradient is 52 °C/cm; the rate of interface growth is about 0.75 μm/s.

eoimaging with two views of the same area is enhanced by this parallax effect.

The source used for the *in situ* experiments had a spot size of approximately 5 μm. The detector technology can show features, such as the solid-liquid interface, with contrast values as low as 2 pct. Real-time viewing is possible by employing an X-ray image intensifier and a cooled CCD camera. With such an arrangement, indium particles of 30 μm have been resolved in real-time observations. Recent advances in X-ray source technology have allowed us to obtain a submicron spot size providing higher resolution images like the Al-30In radiomicrograph discussed in Section III.

Radiography by projection permits placing the specimen in a furnace between the X-ray camera and the source. The best results are generally obtained when the specimen (in a temperature gradient) is placed as close to the source as possible. This increases the magnification and improves detectability. Immediate concerns with the furnace design result. X-ray transparency of the furnace to X-rays while maintaining a molten state in the metal is required. The difficulty is to safely bring the specimen within millimeters of the X-ray source while maintaining a uniform cross section of 1-mm thickness in both the solid and liquid metal. Transparency is difficult to maintain with conventional materials, because the best image contrast is obtained by using the less penetrating lower energy X-rays (acceleration of 20 to 40 kV). As a consequence, the crucible material selected for the aluminum alloys is boron nitride. Prolonged heating in air of the aluminum alloys in the boron nitride crucibles did not show any contact interactions. The furnace housing was actively water cooled and windows of aluminum foil withstood the heat and offered uniform but small attenuation of the X-ray flux.

The furnace employed for this study is a modified horizontal Bridgman–Stockbarger design operated in air. Translation of the specimen through the temperature gradient at slow velocities allows the interface to remain in the X-ray transparent window for long periods of time. End effects and the limited control of temperature lead to a slow drift of the interface across the window (Figure 3 to Figure 7) during the unidirectional solidification along 2 cm of specimen length. A DC motor-driven screw translator pushes/pulls the specimen in its crucible at rates of 2 to 20 μm/s. Before placement into the furnace, the specimen is cut and formed to fit (at temperature) into the cavity machined into the boron nitride crucible. The crucible lid keeps the molten metal at the uniform thickness of 1 mm. The aluminum alloys studied oxidize slowly enough that little additional oxide forms even during hours of being molten. Defects in the alloy such as cracks, shrinkage cavities, holes, *etc.* do not collapse as one might imagine and are clearly visible during radiography. Nonuniformities of solute distribution in the specimen can be detected prior to the experiments by direct X-ray evaluation.

The sample was prepared at the monotectic composition. We checked that the composition was not hypermonotectic by melting back the interface, maintaining zero growth rate for a period of minutes, and noting that no detectable L_2 (indium-rich) droplets were formed in the liquid adjacent to the solid/liquid interface.

III. RESULTS

The results presented here were obtained from one specimen of monotectic Al-In. Conditions of exposure, X-ray energy, and growth rate were repeatedly adjusted to determine the ranges of the parameters that would produce the best results. The power of real-time observation allowed rapid optimization to yield results of fundamental interest.

Figures 3 through 7 show radiomicrographs of the melt/solid interface and surrounding alloy while solidification progresses from right to left. Indium-rich liquid droplets form (Figures 3 through 5 and 7) in the melt near the solid/liquid interface. These droplets usually are engulfed by the solid and can be observed throughout this transition. Variations in absorbance of the X-rays through the solid (Figures 3, 4, 6, and 7) are the direct result of growth rate changes that alter the degree of solute rejection. Buildup of solute (indium) in the melt at the interface is observed in Figure 6 after a step increase of growth rate steepens the concentration gradient of the solute adjacent to the interface. With sufficient accumulation of this solute, nucleation and coalescence of the indium-rich droplets occur (Figure 7). As the droplets grow in the melt and ultimately become engulfed, the solute concentration in the melt diminishes and a steady-state condition develops.

Other features require explanation. For example, the dark transverse lines growing into the melt from the interface (Figures 5 through 7) are pre-existing cracks becoming filled with the indium-rich liquid collecting at the interface.

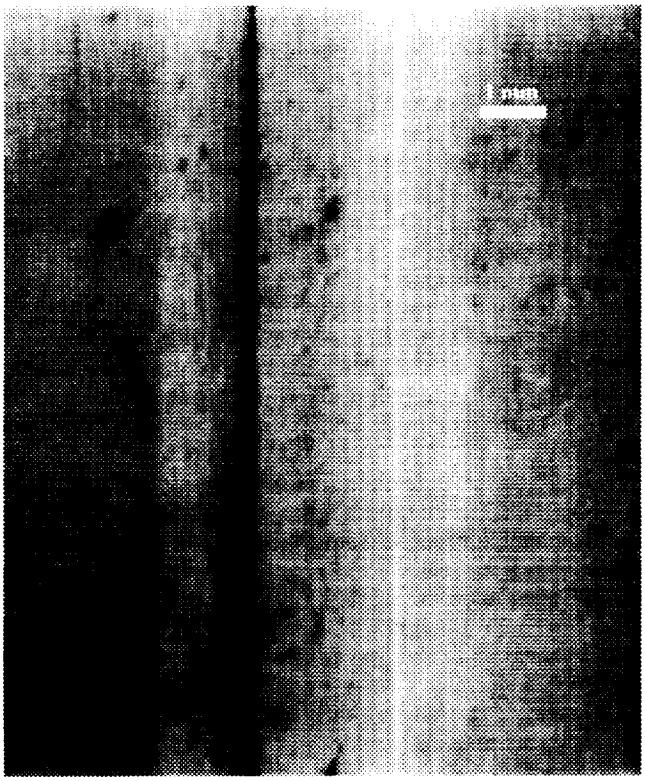

Fig. 4—Solidification rate is 6.5 μm/s. The dark band is a dense layer of indium-rich droplets that decorate the interface since it is stationary for a few minutes. Again, droplets of indium-rich L_2 are seen forming in the melt.

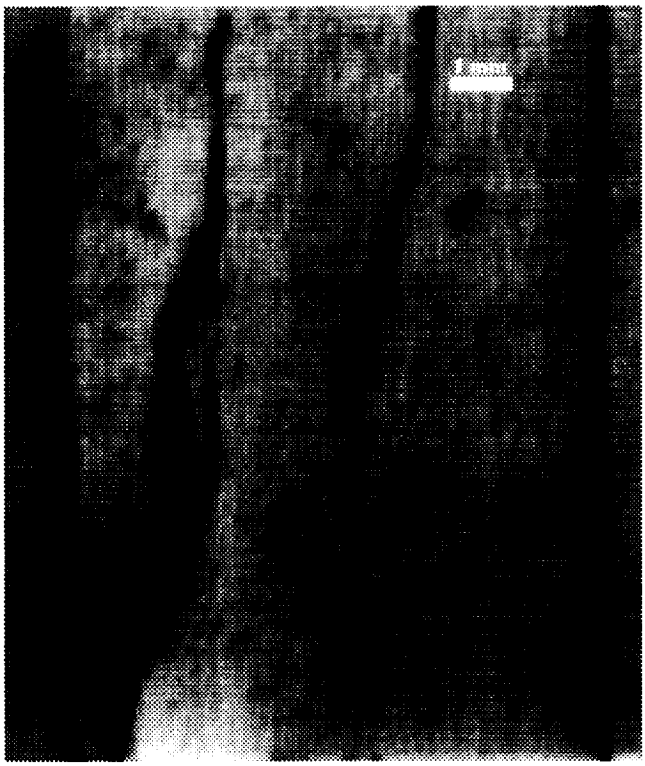

Fig. 5—Solid/liquid interface on the left side shows droplets forming in the melt at 9.1 μm/s solidification rate. Dark, irregular streaks are cracks in the casting filled with L_2, which preferentially wets the interior of these cracks. The streaks fill before the solid/liquid interface reaches them.

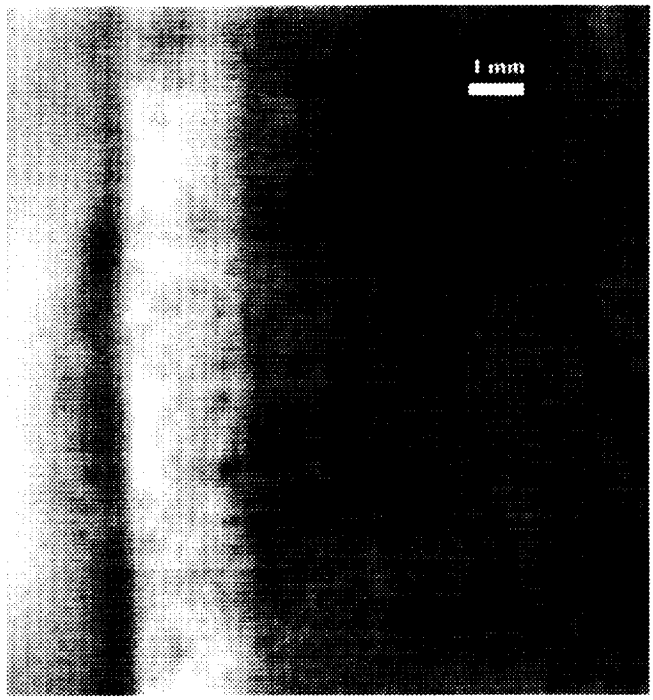

Fig. 6—Interface growing with the 45 °C/cm gradient at the 12.4 μm/s rate after a prior rate of 4 μm/s. The light band is the higher growth rate solid. In response to the growth rate transient, an irregular solute cloud forms in the melt at the interface.

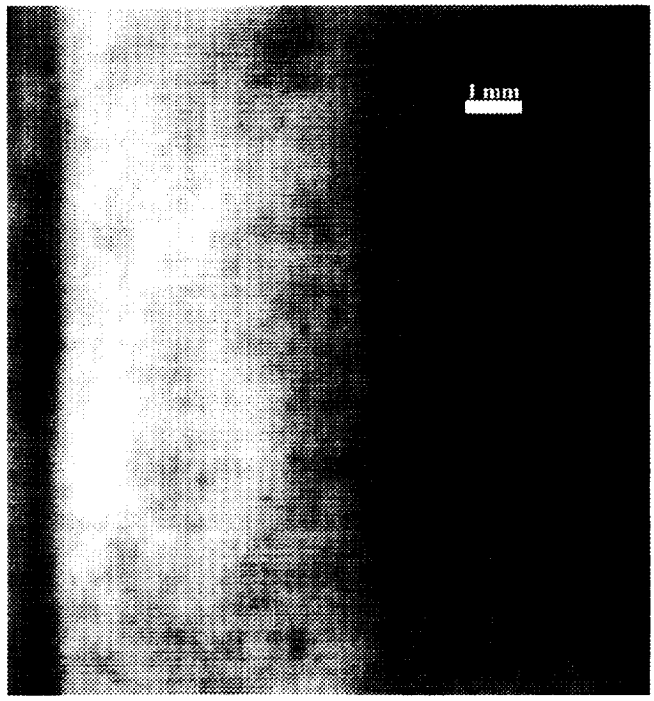

Fig. 7—Same as Fig. 6, at a later time. Solute continues to build up until droplets of L_2 begin to form. Droplets of L_2 formed in the melt during the 4 μm/s growth are seen engulfed by the more rapidly grown, lighter matrix phase. Few droplets are found engulfed in the solid growing at the higher velocity after the first 750 μm.

The indium wets the crack surfaces and is essentially removed from the process. Another interesting feature is the (light-shaded) band depleted of indium that formed during

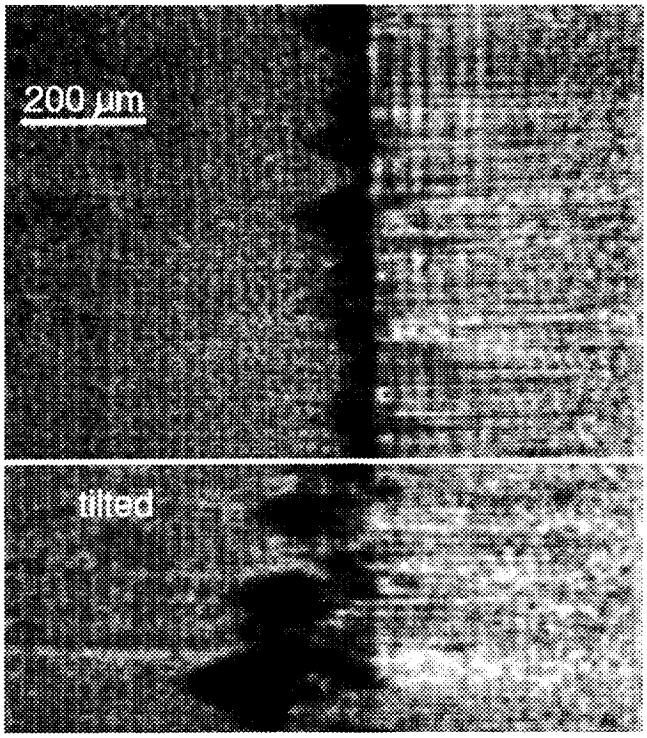

Fig. 8—Postsolidification radiomicrographs of the dark band region shown in Fig. 4. The upper portion has the X-ray beam normal to the growth direction and shows the striations or bands that formed during the slow gradient freeze. The lower image shows the same area with the beam axis at a 35 deg tilt to reveal the discrete particulate nature of the dark band. The large particles are uniformly distributed throughout the depth of the band. The growth direction is to the left.

the first melt-back cycle (Figures 3 and 4). The interface was held stationary at that location for several minutes before growth started. Over time, the aluminum matrix rejected indium by diffusion, leaving the light-shaded, aluminum-rich band through the specimen thickness. Slow growth by gradient freeze from this location resulted in strong solute buildup at the interface. Then, growth slowed to a stop where large droplets of indium formed to create a heavy band of X-ray absorption (Figure 4). In cross section, the degree of absorption leads one to think that a solid band of indium has formed. However, examination of the specimen by X-ray microscopy at an angle to the face of the band reveals, as shown in Figure 8, that it is in fact an array of particles of indium distributed across what was previously the interface.

Higher magnification, with the sample surface again perpendicular to the beam axis, reveals that directly behind this array of particles is a series of bands or striations (Figure 8) caused by the slow growth of the interface.

Recently, we obtained XTM images revealing new features within samples from previous parabolic flight experiments.[8,10] Figure 9 is a film radiograph of a very hypermonotectic specimen grown during repetitive high- and low-gravity cycles on the KC-135 aircraft. This specimen was prepared for the work cited in References 8 and 10. Regions (equivalent in length to the specimen diameter) with few indium particles along the specimen are displayed separating slightly longer regions where significant clustering of the large (200-μm) indium particles has occurred. Similar clustering was observed in other Al-In alloy specimens grown in this manner. Periodic clustering of large indium particles was not observed in control samples grown in normal gravity, so we infer that the periodic variation is a response to the cyclic acceleration pattern. Typically, acceleration cycles during the parabolic maneuvers are 20 seconds at 0.01 g (1 g = 9.80 m/s^2) and 60 seconds at 1.8 g. We show this specimen as an example of the value of the XTM for postsolidification metallography. This pattern of particles was not as obvious from the standard optical metallography performed.[8] In fact, there were no particle clusters of the type visible in the single section optical micrographs.

The second part of Figure 9 shows a magnified view of the small region at the start of growth where the local growth rate was very small. Once again, fine striations parallel to the interface are visible. Only with the application of XTM were these features observed.

IV. DISCUSSION

A. *Concentration Detection Limits*

To enable detection of features such as the solid/liquid interface or the solute boundary layer, differential X-ray absorption within the specimen must provide at least 2 pct contrast. Ignoring camera/converter feature size contrast limitations, we can model the minimum detectable indium concentration. Source flux data for the conditions of our X-ray source,[27] 100 kV acceleration, and a tungsten target, with 1-mm Al filtration, were used for the 10- to 100-keV spectrum range. Adsorption coefficient data[28] were used to calculate the transmitted flux for different indium concentrations in a 1-mm-thick Al sample using Beer's law:

$$I = I_0 \exp(-\mu t) \qquad [2]$$

where I is the intensity after transmission through the specimen, μ is the linear absorption coefficient, and t is the thickness. Figure 10 gives the difference in intensity, I, relative to pure Al for 1 pct by volume indium and Pb. The Pb curve is provided for comparison purposes. For the simple case where our detector detectivity is invariant with X-ray energy, we obtain a value for image contrast by integrating the intensity difference curve from 10 to 100 keV. By iteration with different solute contents, we find that the indium concentration that provides 2 pct contrast is about 0.5 wt pct. This represents the limit of sensitivity that we would expect for imaging diffuse features like the solute boundary layer and excludes spatial resolution arguments.

B. *Particle Size Detection Limits*

The finest resolvable feature size is of the order of the X-ray source spot size, which for these experiments, was 5 μm. (We have recently obtained an X-ray source showing micrometer resolution.) However, typical X-ray image intensifiers or converters (Figure 1) degrade detectability as an inverse function of feature size. This limit of contrast by feature size is measured and known as the modulation transfer function (MTF) of the camera/converter system. A simple interpretation of the MTF is that it represents the ratio of the outgoing signal to the incoming signal. Large features with high contrast (100 pct) will produce a signal

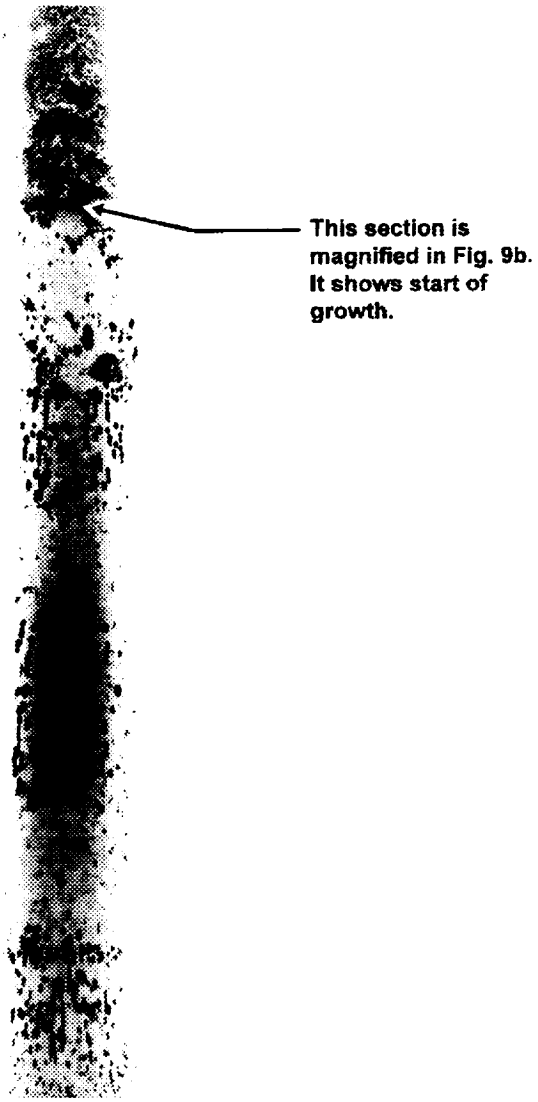

(*a*)

(*b*)

Fig. 9—Microradiographs of the Al-30In hypermonotectic alloy solidified during parabolic flight on the NASA KC-135. The growth rate is 83 μm/s; the temperature gradient is 150 °C/cm. (*a*) The full specimen (5-mm-diameter) view. The periodic clustering of indium particles (typically, 200 μm in diameter) is clearly seen in three regions. The Topmost portion shows unmelted, parent metal and the start of growth during the first low-gravity period. Fig. (b) shows an enlargement of this section. (*b*) Microradiograph of the Al-30In hypermonotectic alloy solidified during parabolic flight on the NASA KC-135. The growth rate is 83 μm/s; temperature gradient is 150 °C/cm. A high magnification view of an area in (a) is shown here. The striations (horizontal) in this specimen can clearly be seen. They are only observed by XTM.

of nearly 100 pct MTF. Tiny features, again with 100 pct contrast, when passed through the system in question, may produce only a 5 pct contrast on the output. The spatial relation is characterized in terms of line pair/cm, where more lines means smaller features. For these experiments, we used a Thompson CSF X-ray Image Intensifier. The manufacturer's MTF for this device is given in Figure 11. Clearly, as the features become smaller, even though they have a full 100 pct contrast to start, output contrast falls rapidly. The added contribution to poor image quality is compounded by the fact that most specimen features do not produce a high contrast input signal. With this information, we can predict the minimum detectable indium particle size from the absorption model and a minimum contrast threshold of 2 pct. For the solidification experiments (Figures 3 through 6), the magnification at the image converter was 5 times. A 2 pct detection limit of 125 μm particles could be obtained at unity magnification. Thus, we expect the minimum resolvable indium particle to be 25 μm. This compares well to the experimentally measured value of 30 $\pm$ 10 μm.

C. *Striations*

Fine, parallel stripes or bands that appear to be localized regions alternating between high and low solute concentrations were found during postsolidification inspection of the Al-In specimen. These striations are shown in Figure 8. The bands were formed during the slow growth that ultimately created the "black" stripe of indium seen in Figure 3. The bands are only visible when the X-ray beam is normal to the band itself. These bands have been previously observed in Al-Pb monotectic solidification structures (again only by X-ray microscopy).[26] By direct experimental observation, the striations could not be related to any growth rate fluctuations. Optical examination of the metallographically prepared specimen revealed no such banding nor distribution of particles that might cause such a band structure. It is clear that the banding is a bulk phenomenon visible only when the band absorption is maximized by viewing along the band surface. Since a low magnification was used, the indium bands shown here (Figure 8) are so faint that they were not observed during formation. One marked obser-

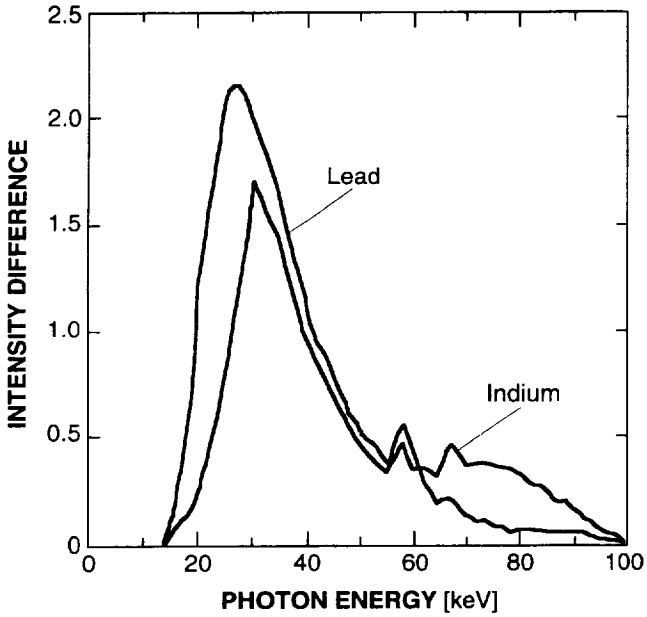

Fig. 10—Plots of the difference in absorption to the incoming 100 kV X-ray spectrum (generated by a tungsten target) of 10 μm of indium or Pb to 1 mm of Al as a function of X-ray photon energy.

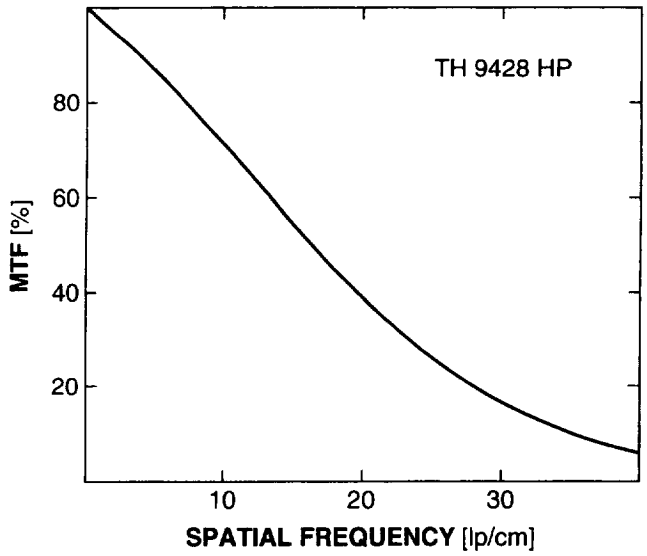

Fig. 11—Modulation transfer function plot for the Thompson CSF X-ray image intensifier tube used in the XTM. Note how the relative contrast (pct MTF) of the image deteriorates as the features become smaller (larger line pairs/cm or lp/cm).

vation from the Al-Pb experiments[26] was that the band structure, while close to the interface, did not reproduce the interface shape itself. Instead, the bands formed at small angles to the interface, creating irregular, wavy parallel stripes in comparison to the smooth, flat solid/liquid interface next to them. Bands formed with a shorter wavelength of irregularity than the interface morphology from which they formed. This raises the caution that striations in a solidified crystal may not, as has been assumed,[29] decorate the interface position and shape.

D. *Solute Segregation*

The indium concentration in the solid and the melt can be directly related by Eq. [2] to the transmitted X-ray intensity recorded on the radiomicrographs discussed in Section C. Figures 6 and 7 clearly show a solute depletion band in the solid resulting from the increase of growth velocity from 4 to 12 μm/s. From traditional theory,[30] one expects that a solute-rich band might form, which is opposite to the experimental result. The equilibrium phase diagram shows indium has insignificant solid solubility in aluminum. In Figure 6, a transient diffuse solute boundary layer is present that formed after the growth rate was increased from 4 to 12 μm/s. A solute layer was not found just after the rate was increased. In fact, it took tens of seconds of solidification to develop the solute cloud in the figure. It is important to note that the isoconcentration lines of solute boundary layer are not parallel to the growth interface as is assumed by most theories. Eventually, the solute builds up to the point where L_2 particles nucleate and grow, subsequently depleting the solute layer of indium.

The indium particles are not observed to be pushed by the solidifying interface. Thus, it is reasonable to postulate that incorporation of indium into the solid is limited by the kinetics of L_2 nucleation and growth. What droplets were present at the interface at the time of the step increase in growth rate were quickly incorporated, as can be seen in the first 750 μm of fast growth in Figure 7. The light band of solid represents the low concentration of indium incorporated due to the lack of available L_2 droplets. Since the growth rate is too high to permit nucleation and growth of the droplets from the solute accumulating at the interface, sufficient growth and rejection of solute must occur to saturate the melt sufficiently to drive droplet nucleation and growth. Until this occurs, there are no L_2 droplets to incorporate and the solid is more transparent to X-rays in comparison to the solid grown previously at the lower growth rate. These arguments also support the supposition that the solute cloud is not merely a fine dispersion of irresolvable droplets.

E. *Applicability of Coupled Growth Theory to Metallic Monotectic Solidification*

Figures 3, 6, and 7 give direct evidence that the immiscible L_2 nucleates in the solute boundary layer in the melt away from the solid/liquid interface. The L_2 droplets are evenly distributed in the bulk and do not nucleate on the BN crucible or on the specimen surface. We verified the three-dimensional positions of the indium particles during solidification and postprocess by moving the X-ray source across the sample and using parallax.

In addition, solute buildup in the melt did not raise the concentration of solute in the solidifying solid until L_2 droplets could form in the melt first. This observation does not support the interpretation that the alloy had a slightly hypermonotectic composition. These observations are thus direct evidence against the assumption that metallic monotectics necessarily grow in a coupled manner.[31]

V. CONCLUSIONS

1. X-ray transmission microscopy is shown to be capable of imaging solidification of optically opaque metal al-

loys in real time with resolutions of up to 30 μm. These data allow the study of the detailed dynamics of solidification processes, including interfacial morphologies, phase growth in the liquid, coalescence, incorporation of phases into the growing interface, and the solute boundary layer in the liquid.
2. The isoconcentration lines of solute boundary layer are not parallel to the growth interface, as is assumed by most theories.
3. Striations in a solidified crystal may not, as has been assumed, accurately decorate the interface position and shape.
4. Variation in acceleration during solidification of a hypermonotectic alloy was shown by XTM to lead to periodic deposition of large indium particles into clustered regions separated by regions with few large indium particles.
5. Metal monotectic alloys, at the monotectic composition, do not necessarily grow in a coupled manner.

ACKNOWLEDGMENTS

We acknowledge the state of Alabama and the Center for Microgravity Materials Research, University of Alabama, Huntsville, for the initial support to perform the experiments. We also acknowledge William K. Witherow, NASA, MSFC, for producing an image file conversion program. This work was funded by NASA Headquarters Microgravity Science and Applications Division Advanced Technology Program.

REFERENCES

1. H. Huppert: in *Handbook of Crystal Growth, Fundamentals Transport and Stability*, D.T.J. Hurle, ed., North-Holland, Amsterdam, 1993, pp. 743-83.
2. J.J. Favier, J.P. Garandet, A. Rouzaud, and D. Camel: in *Joint Launch + One Year Science Review of USML-1 and USMP-1*, N. Ramachandran, D.O. Frazier, S.L. Lehoczky, and C.R. Baugher, eds., NASA Conference Publication 3272, NASA, Washington, DC, 1994, vol. 1, pp. 27-44.
3. M. Vijayakumar, S.N. Tewari, J.E. Lee, and P.A. Curreri: *Mater. Sci. Eng.*, 1991, vol. A132, pp. 195-201.
4. G.H. Otto: *Proc. 5th Eur. Symp. on Material Science under Microgravity*, Schloss-Elmau, Nov. 5–7, 1984, ESA Scientific & Technical Publications Branch, ESC, Nordwijk, The Netherlands, SP-222, pp. 379–88.
5. D. Langbein: *Proc. Norderney Symp. on Scientific Results of the German Spacelab Mission D1*, Norderney, Germany, Aug. 27–29, 1986, Wissenschaftliche Projekt Führung D1, c/o DFVLR, Koln, Germany, 1987, pp. 101, 102.
6. L.L. Lacy and C.Y. Ang: *Apollo Soyuz Test Project Summary Science Report, Vol. I* NASA SP-412, 1977, NASA, Washington, DC, pp. 403-28.
7. J.L. Reger: *Proc. 3rd Space Processing Symp. Skylab Results, Vol. I.*, Apr. 30–May 1, 1974, NASA, Marshall Space Flight Center, AL, pp. 133-58.
8. P.A. Curreri and W.F. Kaukler: NASA Technical Memorandum NASA-TM-86573, NASA, Marshall Space Flight Center, AL, Nov. 1986.
9. M.K. Wu, J.R. Ashburn, P.A. Curreri, and W.F. Kaukler: *Metall Trans. A*, 1987, vol. 18A, pp. 1511-17.
10. B.K. Dhindaw, D.M. Stefanescu, A.K. Singh, and P.A. Curreri: *Metall. Trans. A*, 1988, vol. 19A, pp. 2839-46.
11. J.B. Andrews, A.C. Sandlin, and P.A. Curreri: *Metall. Trans. A*, 1988, vol. 19A, pp. 2645-50.
12. A.C. Sandlin, J.B. Andrews, and P.A. Curreri: *Metall. Trans. A*, 1988, vol. 19A, pp. 2665-69.
13. *Materials Science on Parabolic Aircraft*, NASA TM-4456, P.A. Curreri, ed., NASA, Marshall Space Flight Center, AL, Mar. 1993.
14. W.F. Kaukler and D.O. Frazier: *J Cryst. Growth*, 1985, vol. 71, p. 340; also appeared in NASA-TM 100317, NASA, Marshall Space Flight Center, AL, Dec. 1987.
15. K.A. Jackson and J.D. Hunt: *Acta Metall.*, 1965, vol. 13, p. 1212.
16. R. Trivedi, J.A. Sekhar, and V. Seetharaman: *Metall. Trans.*, 1989, vol. 20A, pp. 769-77.
17. M.E. Glicksman and C.L. Vold: *Acta Metall.*, 1967, vol. 15, p. 1409.
18. B. Lindstrom: *X-Ray Optics and X-Ray Microanalysis*, H.H. Pattee, V. Cosslett, and A. Engstrom, eds., Academic Press, New York, NY, 1963, pp. 13-22.
19. G. Grange, J. Gastaldi, C. Jourdan, and P. Marzo: *J. Cryst. Growth*, 1992, vol. 121, pp. 315-21.
20. T. Kobayashi, Y. Nishikawa, and T. Imura: *J. Cryst. Growth*, 1987, vol. 84, pp. 489-95.
21. G. Grange, C. Jourdan, and J. Gastaldi: *J. Cryst. Growth*, 1988, vol. 87, pp. 325-30.
22. F.P. Chiaramonte, G.F. Danier, J. Gotti, E.S. Neumann, J. Johnston, and K.J. De Witt: *AIAA 30th Aerospace Sciences Meeting*, Reno, NV, Jan. 6–9, 1992, paper no. 92-0845.
23. P.G. Barber, R.F. Berry, W.J. Debnam, A.L. Fripp, G. Woodell, and R.T. Simchick: *J. Cryst. Growth*, 1995, vol. 147, pp. 83-90.
24. G.R. Chappleman: *J. Mater. Sci.*, 1982, vol. 17, p. 2208.
25. S. Rondot, J. Cazaux, O. Aaboubi, J.P. Chopart, and A. Oliver: *Science*, 1994, vol. 263, pp. 1739-41.
26. W.F. Kaukler and F. Rosenberger: *Metall. Mater. Trans. A*, 1994, vol. 25A, pp. 1775-77.
27. N. Mika and K.H. Reiß: *Tabellen Zur Rontgendiagnostik*, Siemens Aktiengesellschaft, Erlangen, Oct. 1973.
28. *Compilation of X-ray Cross Sections*, UCRL-50174, Sec. II, Rev. 1, University of California, Livermore, CA, 1969.
29. H. Klapper: *Characterization of Crystal Defects by X-Ray Methods*, B.K. Tanner and D.K. Brown, eds., Plenum Press, New York, NY, 1980, p. 147.
30. V.G. Smith, W.A. Tillet, J.W. Rutter, and B. Chalmers: *Acta Metall.*, 1953, vol. 1, p. 428.
31. K.A. Jackson and J.D. Hunt: TMS-AIME, 1966, vol. 236, pp. 1129-42.